Towards all-solution-processed top-illuminated flexible organic solar cells using ultrathin Ag-modified graphite-coated poly(ethylene terephthalate) substrates

Wang, Shuanglong; Zhao, Yi; Lian, Hong; Peng, Cuiyun; Yang, Xuyong; Gao, Yulai; Peng, Yan; Lan, Weixia; Elmi, Omar Ibrahim; Stiévenard, Didier; Wei, Bin; ZHU, Fu Rong; Xu, Tao

[Link to publication]()

Authors

Shuanglong Wang, Yi Zhao, Hong Lian, Cuiyun Peng, Xuyong Yang, Yulai Gao, Yan Peng, Weixia Lan, Omar Ibrahim Elmi, Didier Stiévenard, Bin Wei, Furong Zhu, and Tao Xu

Research article

Shuanglong Wang[a], Yi Zhao[a], Hong Lian, Cuiyun Peng, Xuyong Yang, Yulai Gao*, Yan Peng, Weixia Lan, Omar Ibrahim Elmi, Didier Stiévenard, Bin Wei, Furong Zhu* and Tao Xu*

Towards all-solution-processed top-illuminated flexible organic solar cells using ultrathin Ag-modified graphite-coated poly(ethylene terephthalate) substrates

Abstract: All-solution-processed flexible organic solar cells (FOSCs) with high power conversion efficiency (PCE) are the prerequisite for application in low-cost, large-area, flexible, photovoltaic devices. In this work, high-performance, top-illuminated FOSCs using ultrathin Ag-modified graphite-coated poly(ethylene terephthalate) (PET) substrates are demonstrated. The ultrathin Ag-modified graphite/PET substrates have excellent electric conductivity, mechanical flexibility, and easy processability for FOSCs. A PCE of 5.31% for FOSCs, based on the blend system poly[4,8-bis(5-(2-ethylhexyl)thiophen-2-yl) benzo [1,2-b:4,5-b′]dith-iophene-*co*-3-fluorothieno[3,4-b]thiophene-2-carboxylate]: [6,6]-phenyl-C7l-but-yric acid methyl ester, having a bilayer of MoO_x/Ag upper transparent anode is demonstrated. Top-illuminated FOSCs with a transparent upper electrode of solution-processed Ag nanowires also yielded a PCE of 3.76%. All-solution-processed FOSCs exhibit excellent mechanical flexibility and retain >81% of the initial efficiency after 500 cycles of bending test. Furthermore, graphite-based electrodes demonstrate good heat-insulation properties. The outcomes of this work offer an alternative to fabricate high-performance, all-solution-processable, top-illuminated FOSCs, providing a commercially viable approach for application in large-area solar cells that can be prepared by printing and roll-to-roll fabrication processes.

Keywords: Ag-modified graphite; flexible organic solar cells; top-illuminated; all-solution-processed.

[a]**Shuanglong Wang and Yi Zhao:** These authors equally contributed to this work
*Corresponding authors: Yulai Gao, School of Materials Science and Engineering, Shanghai University, Shanghai 200072, China, e-mail: gaoyl@shu.edu.cn; **Furong Zhu,** Department of Physics and Institute of Advanced Materials, Hong Kong Baptist University, Kowloon, Hong Kong, China, e-mail: frzhu@hkbu.edu.hk; and **Tao Xu,** School of Mechatronic Engineering and Automation, Key Laboratory of Advanced Display and System Applications, Ministry of Education, Shanghai University, Shanghai 200072, China, e-mail: xtld@shu.edu.cn
Shuanglong Wang, Yi Zhao, Cuiyun Peng, Xuyong Yang, Yan Peng, Weixia Lan and Bin Wei: School of Mechatronic Engineering and Automation, Key Laboratory of Advanced Display and System Applications, Ministry of Education, Shanghai University, Shanghai 200072, China
Hong Lian: MOE Key Laboratory for Interface Science and Engineering in Advanced Materials and Research Center of Advanced Materials Science and Technology, Taiyuan University of Technology, 79 Yingze West Street, Taiyuan 030024, China
Omar Ibrahim Elmi: IEMN, UMR8520, Université de Lille1, 59652 Villeneuve d'Ascq Cédex, France; and Université de Djibouti, Faculté des Sciences BP 1904, City of Djibouti, République de Djibouti
Didier Stiévenard: IEMN, UMR8520, Université de Lille1, 59652 Villeneuve d'Ascq Cédex, France

1 Introduction

Flexible organic solar cells (FOSCs) with a bulk heterojunction (BHJ) structure are considered to be the next-generation renewable and clean energy conversion technology because of their advantages of mechanical flexibility, light weight, rapid energy payback time, and low-cost solution fabrication processability [1–4]. FOSCs with a regular cell structure are often made on indium-tin-oxide (ITO)-coated poly(ethylene terephthalate) (PET) and transparent, flexible plastic substrates, and have reasonably good visible light transparency, proper work function, and good conductivity [5–8]. However, ITO-based flexible transparent substrates have some limitations because the ITO electrode is fragile and indium is not abundant on earth, restricting its potential for application in large-area, flexible solar cells [9, 10]. Therefore, there is an urgent need to develop an alternative technology to replace ITO for FOSCs. Different materials have been investigated, including carbon nanotubes, graphene, conducting polymers, and metallic nanowires (NWs) [11–14].

Another promising strategy to overcome the aforementioned limitations is to develop FOSCs with a top-illuminated

cell architecture using an opaque, flexible substrate and a reversal of the illumination direction [15], using, e.g. stainless steel foils, paper, or textiles, for making flexible solar cells [16–18]. In top-illuminated FOSCs, the cathode or the electron extraction layer (EEL) is below the BHJ, resulting in stable device performance [19]. A top-illuminated OSC with a power conversion efficiency (PCE) of 1.04%, which is based on the blend of poly(3-hexylthiophene):[6,6]-phenyl-C61-butyric acid methyl ester (P3HT:PC$_{61}$BM), using a pair of upper thin Ag films and a bilayer Al/AgO$_x$ bottom electrodes, has been reported [20]. Jung et al. developed a nanostructured, back-reflective Ag electrode for enhancing the efficiency of top-illuminated OSCs. On incorporating plasmonic-assisted electrodes into the P3HT:PC$_{61}$BM blend system, the cell efficiency increased from 2.91 to 3.35% compared to devices using a planar bottom electrode [21]. A dielectric/metal/polymer top transparent electrode, with a low-refractive-index poly(dimethylsiloxane) (PDMS) optical out-coupling layer, for top-illuminated FOSC with a PCE of 6.75%, based on the polythieno[3,4-b] thio-phene/benzodithiophene:[6,6]-phenyl-C70 butyric acid methyl ester blend system, was also reported [22]. However, employing the Ag bottom electrode is still a limitation for fabricating FOSCs with its inherent shortcomings such as the relatively brittle nature of the thin Ag contact, easy oxidation, and the involvement of high-cost fabrication processes [23].

A graphite-coated PET substrate is an attractive candidate for high-performance, flexible optoelectronic devices because of its good electrical conductivity, excellent mechanical flexibility, heat rejection, and chemical stability, and low cost [24–26]. However, direct use of graphite/PET has some limitations such as its low reflectivity. Therefore, further efforts are needed to modify the surface properties of the graphite/PET substrate before it can be used for application in top-illuminated FOSCs. This aside, the efficiency of the top-illuminated FOSCs reported today is still relatively low compared with that of the FOSCs with a regular device configuration [20, 27, 28]. In addition, it is reported that heat rejection of solar cells plays an important role in the overall performance of photovoltaic-based devices and can significantly affect the overall heating, lighting, and cooling costs of a building [29–31]. It is therefore necessary to get deep insight into the heat-insulation properties of graphite-based electrodes.

In this work, we report our effort to develop high-performance, top-illuminated FOSCs using a combination of a PDMS-Ag-nanowire (Ag NWs) upper transparent electrode and an ultrathin Ag-modified graphite-coated PET substrate. A PCE of 5.31% was achieved for the top-illuminated FOSC having a 12-nm-thick Ag upper electrode. More encouragingly, a PCE of 3.76% was obtained for all-solution-processable FOSCs with a PDMS/Ag

NWs transparent upper electrode, based on a blend of poly[4,8-bis(5-(2-ethylhexyl) thiophen-2-yl)benzo[1,2-b:4,5-b']dithiophene-*co* -3-fluorothieno[3,4-b]thiophene-2-carboxylate]:[6,6]-phenyl-C7l-butyric acid methyl ester (PTB7-Th:PC$_{71}$BM) system. The all-solution-processed, top-illuminated FOSCs, fabricated at a low process temperature, exhibited an open-circuit voltage (V_{oc}) of 0.76 V, a short-circuit current density (J_{sc}) of 7.83 mA/cm², and a fill factor (FF) of 63.24%. The all-solution-processed devices with a PDMS/Ag NWs upper contact also exhibited much improved operation stability and high mechanical flexibility compared to FOSCs with a vacuum-prepared bilayer MoO$_x$/Ag (12 nm) transparent upper electrode, retaining over 81% of the initial PCE after 500 cycles of bending tests (bending radius, $r = 4$ mm), giving a promising approach for large-area FOSCs that can be prepared using blade-coating and roll-to-roll manufacturing techniques. Finally, the heat-insulation properties of graphite-based FOSCs were studied, which resulted in better performance compared to that of the commonly used Ag electrode.

2 Results and discussion

2.1 Characterization of the ultrathin, Ag-modified graphite electrode

Figure 1A shows the overall fabrication process of the ultrathin, Ag-modified graphite electrode. The performance of the top-illuminated FOSC was optimized by adjusting the thickness of the ultrathin Ag layer deposited on the graphite electrode. Figure 1B and C shows the reflectivity and the corresponding sheet resistance of graphite electrodes as a function of the thickness of Ag modification layer (0, 0.5, 1, and 2 nm). The inset of Figure 1C shows a photo taken of a bent graphite film. The ultrathin, Ag-modified graphite surface helps in increasing internal reflection, thereby enhancing the absorption in the active layer. A bare graphite film has an average reflectivity of 30.1%, while graphite films modified by Ag films with thicknesses of 0.5, 1, and 2 nm have an average reflectivity of 38.3, 57.9, and 59.4%, respectively, over the wavelength range 400–800 nm. The reflectance spectrum of the Ag film (120 nm) on the PET substrate is shown in Figure S1. The sheet resistance of the ultrathin, Ag-modified graphite, measured with a four-point probe, shows a gradual increase with increase in the Ag layer thickness. As shown in Figure 1C, the bare graphite film has a sheet resistance of 3.55 Ω/sq, while graphite films modified with Ag films of 0.5, 1, and 2 nm have sheet resistances of 3.78, 3.82, and 4.09 Ω/sq, respectively.
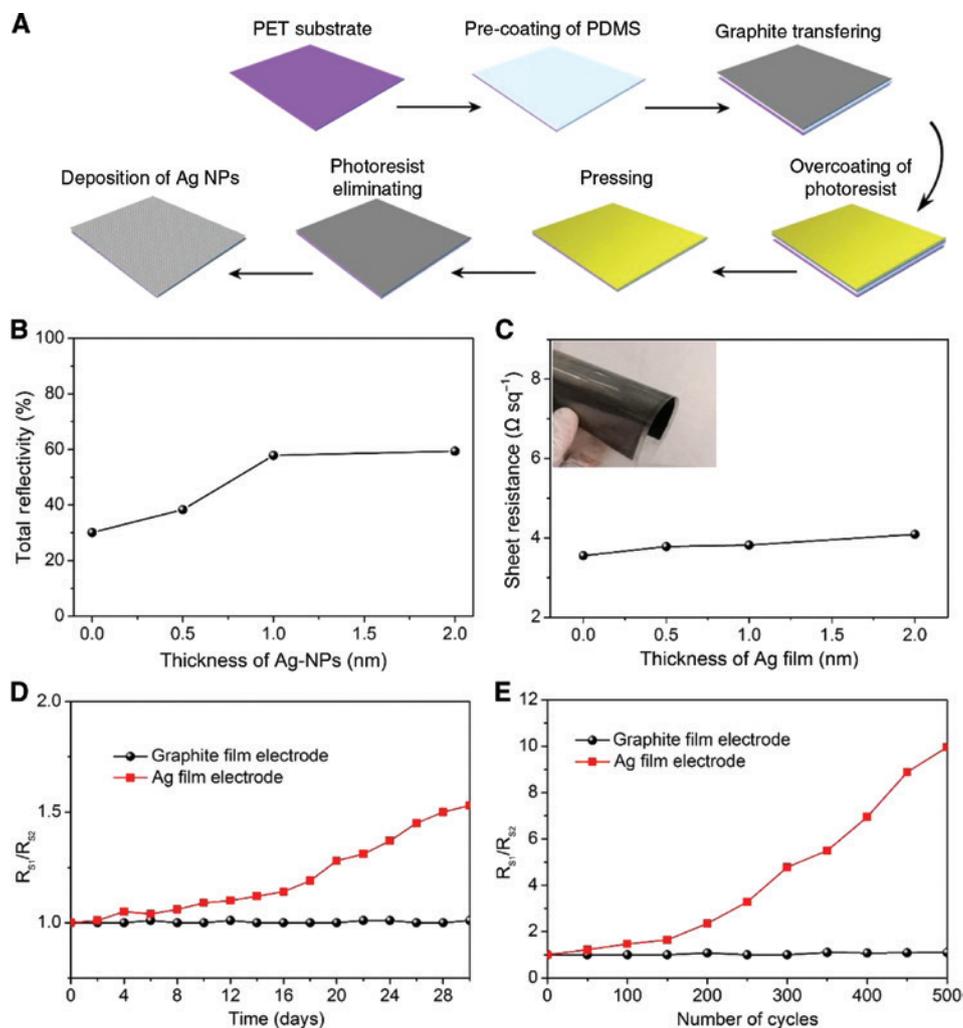
Figure 1: The fabrication process of Ag-modified graphite electrode and characterisation.
(A) Schematic diagram showing the fabrication procedure of ultrathin Ag-modified graphite bottom electrode. (B) Reflectivity of ultrathin Ag-modified graphite films as a function of the Ag layer thickness. (C) Sheet resistance of ultrathin Ag-modified graphite films as a function of the Ag layer thickness. Inset: Photograph of a graphite film (15 cm × 20 cm). (D) R_s response of graphite and Ag films on PET substrate with air exposure (room temperature) for 30 days. (E) Dependence of resistance of the electrode on the number of bending cycles. R_{S1} and R_{S2} correspond to the resistance before and after bending, respectively.

An ideal opaque bottom electrode with high light reflectivity across the visible spectrum and high conductivity for charge extraction is desired for FOSCs [32, 33]. Therefore, to balance the sheet resistance with the optical reflectivity, we defined a figure of merit (FOM), which was introduced to characterize the optical and electrical performance of the opaque bottom electrode; it is defined as $Q_{FOM} = R_f/R_s$, where R_f is the reflectivity and R_s is the sheet resistance [34, 35]. Q_{FOM} for a bare graphite film was $0.85 \times 10^{-1}/\Omega$, while the Q_{FOM} for 0.5, 1, and 2 nm ultrathin Ag-modified graphite films were 1.01×10^{-1}, 1.52×10^{-1}, and $1.44 \times 10^{-1}/\Omega$, respectively, as shown in Figure S2. As a result, the graphite electrode modified with 1-nm-thick Ag gave the highest FOM.

As a highly flexible conducting film, this modified, opaque graphite electrode showed excellent mechanical properties, including strong mechanical robustness and good stability in air [36]. It is known that the chemical stability of the electrode films is one of the most important factors determining the performance of FOSCs. As shown in Figure 1D, the change in the conductivity of the graphite film exposed to air over 30 days was monitored by measuring its sheet resistance once for every 2 days. R_s of the graphite electrode showed negligible variation within the entire duration of air exposure, attributable to its excellent chemical stability compared to that of Ag (120 nm)/PET. Furthermore, a bending test was performed, which included convex and a concave compression with a bending radius of 4 mm, and the sheet resistance of the sample was measured every 50 bending cycles. The flexibility of Ag (120 nm)/PET substrate was also tested as reference. The conductance of the
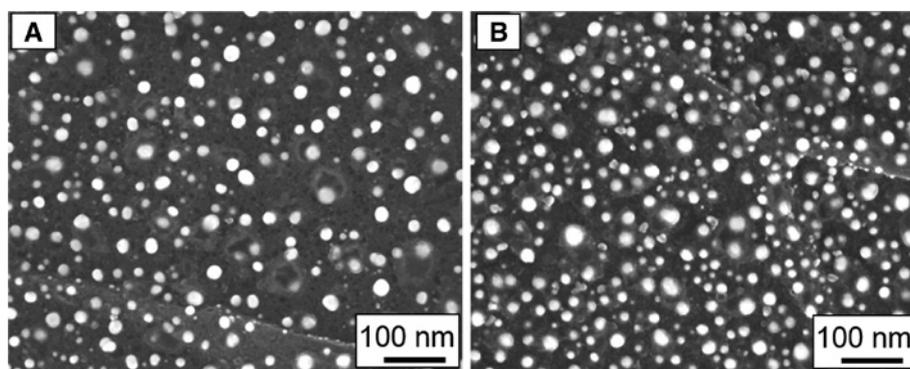
Figure 2: SEM images of the graphite films modified by ultrathin Ag layers with different thicknesses.
(A) 1 nm and (B) 2 nm.

graphite electrode was almost unchanged after 500 cycles of the bending test, while the change in the sheet resistance was <10%, as shown in Figure 1E, indicating good adhesion between the modified graphite film and the substrate, which is resistant to bending fatigue. In contrast, the sheet resistance of the Ag (120 nm)/PET substrate increased significantly compared to that of the thin-film graphite electrode, which increased by almost 10 times after 500 cycles of the bending test. The increase in R_s for the Ag film electrode most likely originated from its brittleness and tiny cracks formed during the bending test.

In order to get further insight into and a better understanding of the morphology of the Ag-modified graphite electrode, the formation of the nanostructured Ag ultrathin films was characterized using scanning electron microscopy (SEM). Figure 2 shows that the ultrathin, Ag-modified layer formed on the surface of the graphite electrode did not result in a continuous film but formed randomly distributed discrete Ag nanoparticles (NPs). Figure 2A shows the reference graphite film with a 1-nm-thick Ag layer. The ultrathin Ag layers tended to form isolated nuclei following the Volmer–Weber growth mode [37]. In this growth mode, Ag–adatom interactions are stronger than the adatom–surface interactions, leading to the formation of three-dimensional adatom islands or NPs. Hemispherical Ag NPs were randomly distributed on the surface of the thin-film graphite electrode, with their diameter ranging from 7.2 to 20.1 nm. Figure 2B shows the graphite substrate with a 2-nm-thick Ag film, where similar Ag NPs were observed with a higher density and a diameter ranging from 7.8 to 26.9 nm.

2.2 Optimization of FOSC device performance

A pair of PTB7-Th: PC$_{71}$BM-based, top-illuminated FOSCs with ultrathin, Ag-modified graphite bottom electrode and a top electrode of the bilayer MoO$_x$/Ag or Ag NWs were fabricated. The cell configurations were as follows: Device A: PET/graphite/ZnO/PTB7-Th:PC$_{71}$BM/MoO$_x$/Ag (12 nm); Device B: PET/graphite/Ag (0.5 nm)/ZnO/PTB7-Th:PC$_{71}$BM/MoO$_x$/Ag (12 nm); Device C: PET/graphite/Ag (1 nm)/ZnO/PTB7-Th:PC$_{71}$BM/MoO$_x$/Ag (12 nm); Device D: PET/graphite/Ag (2 nm)/ZnO/PTB7-Th:PC$_{71}$BM/MoO$_x$/Ag (12 nm); Device E: PET/graphite/Ag (1 nm)/ZnO/PTB7-Th:PC$_{71}$BM/PEDOT:PSS/Ag NWs/PDMS.

Figure 3A shows a schematic of the flexible device architecture as well as the chemical structures of the active materials. Figure 3B shows the J–V characteristics of the top-illuminated FOSCs measured under AM 1.5G illumination. The reference Device A showed a PCE of 3.45% with a V_{oc} of 0.78 V, a J_{sc} of 7.06 mA/cm^2, and an FF of 63.01%. A higher PCE of 3.92% was obtained for Device B using the Ag (0.5 nm)-modified graphite electrode, while that of the Device C with the Ag (2 nm)-modified graphite electrode was 5.20%. The highest PCE of 5.31% was obtained for Device C with the Ag (1 nm)-modified graphite electrode, giving a V_{oc} of 0.77 V, J_{sc} of 10.12 mA/cm^2, and FF of 68.31%. Such results are consistent with the optimized FOM value of the Ag-modified graphite electrode. A summary of the cell parameters measured for different FOSCs as well as the standard deviations of the results obtained by statistical analysis are given in Table 1. The external quantum efficiency (EQE) spectra in Figure 3C reveal that the significant improvement in the entire visible range is responsible for the higher PCE of the FOSCs with the ultrathin, Ag-modified graphite electrode. Considering the same batch processing for the top-illuminated FOSCs, there is substantial improvement in the PCE of the OSCs with the Ag (1 nm)-modified graphite electrode as compared to that of the reference cells; the remarkable increase in J_{sc} can be attributed to a combination of enhanced absorption and suitable electrical conductivity in top-illuminated FOSCs with the Ag (1 nm)/
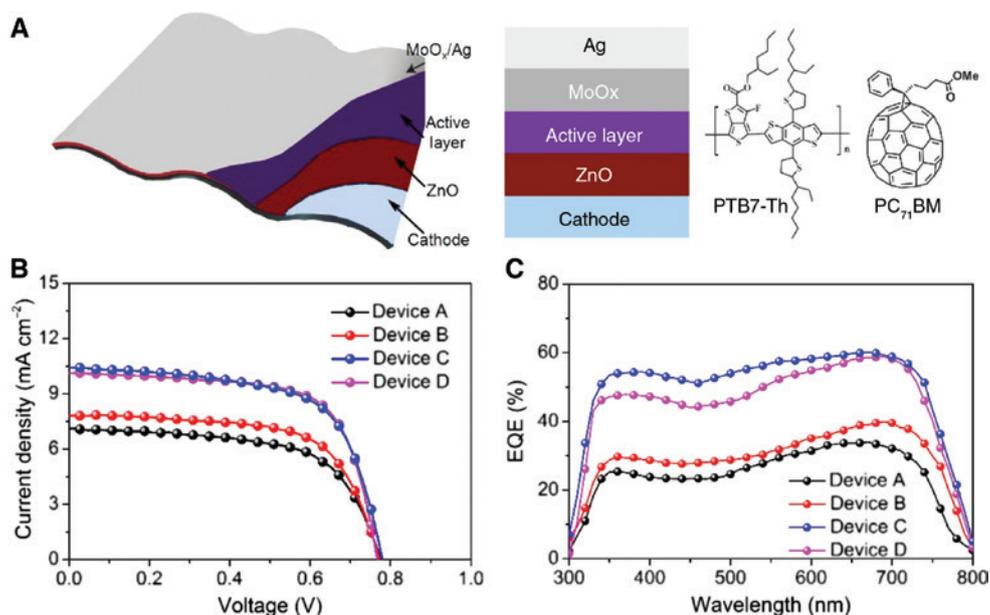
Figure 3: FOSC characteristics.
(A) Schematic illustrations of a top-illuminated FOSC and the molecular structure of the active materials used in this study. (B) *J–V* characteristics and (C) external quantum efficiency (EQE) spectra measured for the top-illuminated FOSCs made with different bottom electrodes of bare graphite (Device A), Ag (0.5 nm)-modified graphite (Device B), Ag (1 nm)-modified graphite (Device C), Ag (2 nm)-modified graphite (Device D).

Table 1: Summary of the cell parameters obtained for different top-illuminated FOSCs.

Device	Ag film (nm)	V_{oc} (V)	J_{sc} (mA/cm²)	FF (%)	PCE$_{max}$. (avg.) (%)
A	0	0.78 ± 0.02	7.06 ± 0.01	63.01 ± 0.02	3.45 (3.24)
B	0.5	0.77 ± 0.03	7.85 ± 0.02	64.49 ± 0.02	3.92 (3.77)
C	1	0.77 ± 0.01	10.12 ± 0.01	68.31 ± 0.05	5.31 (5.18)
D	2	0.76 ± 0.01	10.23 ± 0.03	67.01 ± 0.06	5.20 (5.12)
E	1	0.76 ± 0.02	7.83 ± 0.03	63.24 ± 0.04	3.76 (3.49)

modified graphite bottom electrode. Notably, this is the first report on top-illuminated FOSCs using a graphite-coated PET substrate, delivering the highest PCE for OSCs using the graphite electrode [38–40].

Finite-difference time-domain (FDTD) simulations of the optical absorption versus the different Ag thicknesses deposited on the graphite substrate were performed to get a better understanding on the influence of the Ag NPs on the absorption of light in the active layer. We have taken as reference the incident flux of light after the Ag NW film and the MoO$_x$ layer. The key point is what happens after these layers, i.e. what is the influence of the decorated graphite back-contact on the absorption in the active layer versus the plasmonic effects (i.e. local electric field enhancement) around the Ag NPs. Finally, we assumed that no light is reflected at the graphite–air interface (there is 2.5% absorption per atomic plane for graphite) and added a PML (perfectly matched layer) at the rear face of the structure. SEM

analyses of the Ag NP arrays versus the initial Ag thickness allowed us to measure the average distance between the Ag NPs as well as their diameters. Figure 4 gives the evolution of the light absorption in the active layer versus the Ag NP arrays. Compared to the bare graphite, better absorption is observed between 400 and 700 nm, which is in agreement with the previous EQE measurements.

Two peaks appear around 500 and 625 nm in the absorption spectrum of Figure 4, which are associated with surface plasmon (SP) resonance of individual and coupled Ag NPs. The contribution of individual and coupled Ag NPs depends on the distribution of Ag NPs. Based on simulation of Karg et al. [41], the peak around 500 nm could be attributed to SP resonance of a single NP, whereas the other one, around 625 nm, could be attributed to coupled NPs. For single NPs, the resonance frequency varies with the NP diameter, with a red shift as the diameter increases. Our simulation has been performed with
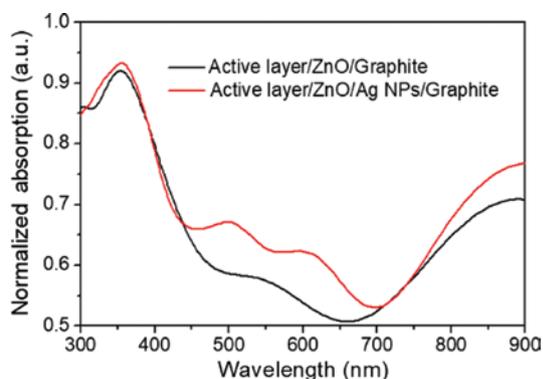
Figure 4: Simulated optical absorption calculated in the active layer for devices A and C.

a diameter of 11 nm for Ag NPs (the average value deduced from Figure 2), but there is also contribution to lower and higher frequencies since the diameter distribution of the Ag NPs ranges from 7.2 to 20.1 nm. For coupled NPs, the resonance could vary from 400 to 600 nm [41]. Therefore,

the contributions of single and coupled NPs overlap. Moreover, An et al. [42] have studied the SP effect in top-illuminated polymer solar cells with nanostructured Ag rear electrodes. Several times enhancement of the absorption around 400 and 550 nm was observed, which was attributed to SP resonances that confine the light within the active layer. They showed the local enhancement of the electric field around the NP and in the active layer, leading to the same conclusion given in this work.

On the basis of the above results, a pair of Ag (1 nm)-modified graphite bottom electrode and a solution-processed, PEDOT:PSS-modified Ag NWs/PDMS upper transparent electrode were optimized for the top-illuminated FOSCs. The spectral transmittance of the transparent electrode with Ag NWs and PDMS coated on PET substrates is shown in Figure S3. The PEDOT: PSS hole extraction layer was adopted. The SEM image of Ag NWs/PDMS upper contact is shown in the inset of Figure 5A. The typical *J*–*V* characteristics and the EQE measured for the top-illuminated FOSCs (Device E) are shown in
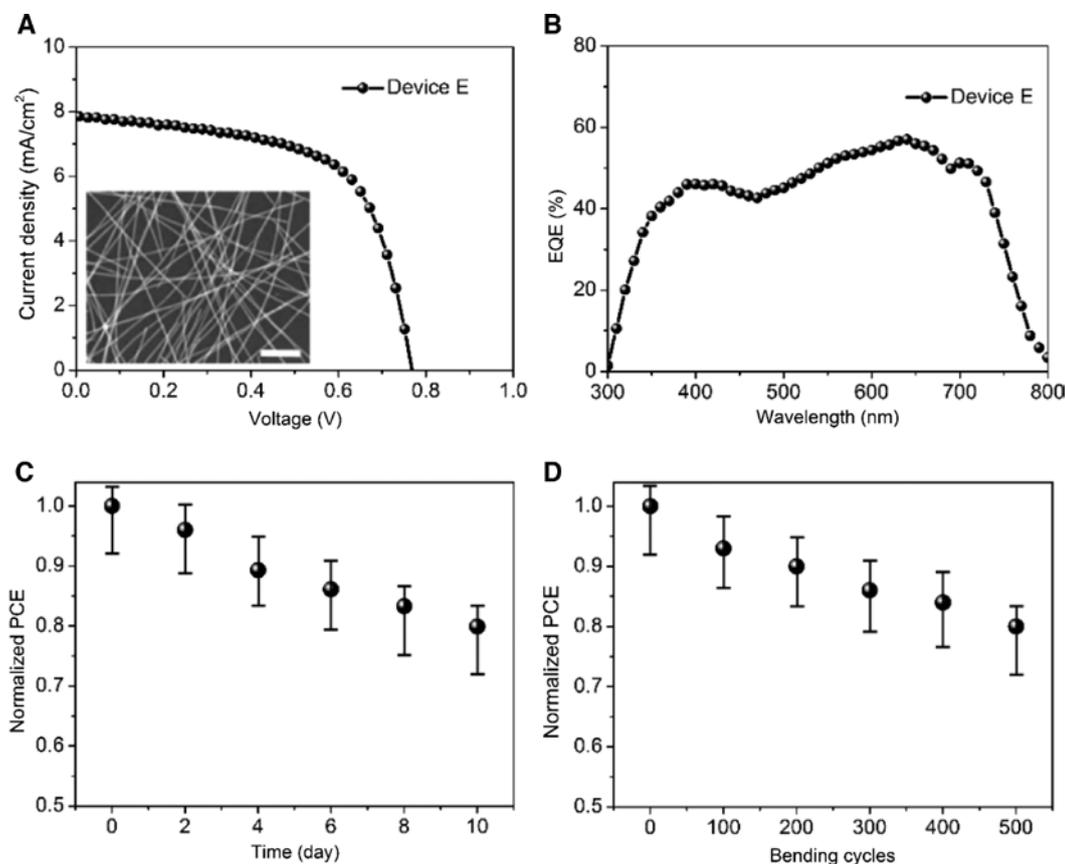

Figure 5: Device E characteristics.
(A) *J*–*V* characteristics and (B) EQE spectra measured for the FOSCs with a pair of Ag (1 nm)-modified graphite bottom electrode and a solution-processed PDMS-Ag NW upper transparent electrode (Device E). The inset shows the SEM image of the Ag NW upper electrode. The scale bar is 1 μm. (C) Normalized PCE of Device E as a function of the aging time, measured for the cells stored in air. (D) Normalized PCE of Device E as a function of the number of the bending cycles.

Figure 5A and B, respectively. The devices yielded the best PCE of 3.76% with a V_{oc} of 0.76 V, J_{sc} of 7.83 mA/cm², and FF of 63.24%. Such results are very encouraging when compared to previously reported results [30, 43]. Statistical results of the device performance are provided as histogram charts in Figure S4. It is anticipated that the all-solution-processed FOSCs will offer an opportunity for large-area solar cells fabricated through printing and roll-to-roll manufacturing processes [44, 45].

2.3 Stability, flexibility, and heat insulation properties of FOSCs

Long-term stability is of crucial concern for practical application of organic photovoltaic devices. The air stability of the top-illuminated FOSCs made with an Ag NW/PDMS upper electrode was examined, with the devices being kept under air conditions in the dark, as shown in Figure 5C. The device exhibited superior air stability, retaining almost 80% of its initial PCE after exposure to air for an extended period of over 10 days. The use of the upper PDMS layer in the FOSCs is favorable for improved operation stability, creating a barrier that protects the underlying functional layers and preventing moisture ingress, leading to slow degradation. The all-solution-processed, top-illuminated FOSCs also retained over 81% of their initial PCE during the bending test using a radius of 4 mm convex and concave compressions for 500 bending cycles, as shown in Figure 5D.

Finally, we went one step further to evaluate the capability of the graphite electrode for reducing the temperature under illumination. An infrared lamp was used to heat a thin metal object, while a PET substrate coated with Ag film (120 nm), graphite film, or a top-illuminated FOSC device was placed between the lamp and the metal to test the heat-insulation properties of different electrodes. Thermal images of the metal were recorded using an infrared camera, which are shown in Figure 6. After the same illumination, the temperature of the metal object reached approximately 35.2°C when the Ag electrode/PET was used, while it became almost 10% lower at 31.6°C for graphite electrode/PET. The thermal conductivity coefficient for the graphite electrode ($\kappa_{graphite} = 100–150$ W/m K) is much lower than that of Ag film ($\kappa_{Ag} = 429$ W/m K), so the heat-insulation property of the graphite electrode is better than that of the Ag electrode. Finally, the graphite-based, top-illuminated FOSC device gave a temperature of 31.3°C, confirming the good heat-insulation property of the graphite electrode. These results illustrate that the proposed graphite-electrode-based, top-illuminated FOSCs can effectively reduce the solar heat flux and can potentially be used as a power-generating and heat-control device by sticking them to the walls to provide electricity and also keep the interior temperature of buildings low.
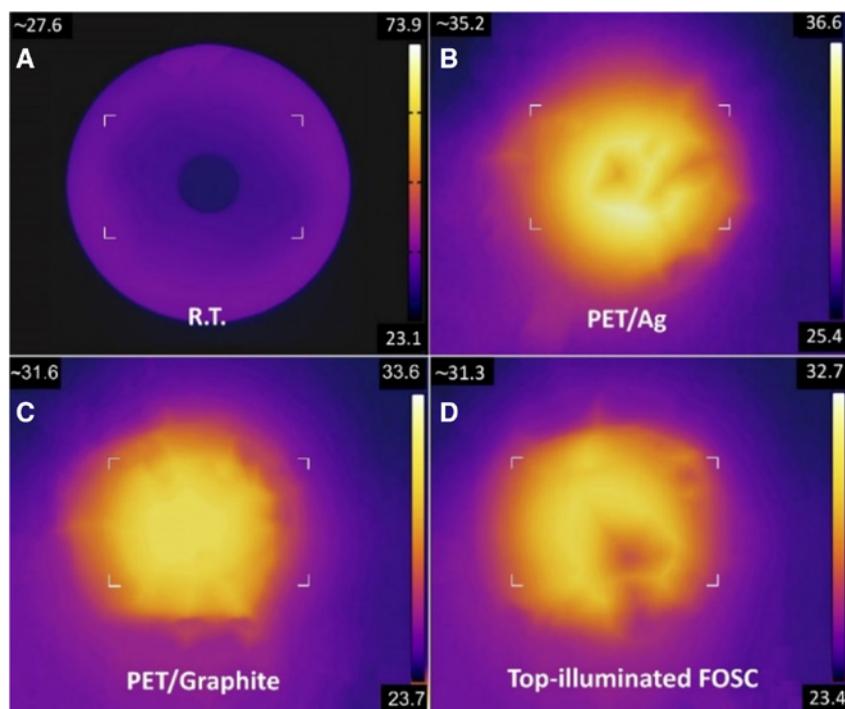

Figure 6: Thermal images taken with an IR camera for comparing the heat-insulation properties.
(A) Thin metal object. (B) PET/Ag substrate. (C) PET/Graphite substrate. (D) Top-illuminated FOSC.

3 Conclusions

In conclusion, we have investigated graphite films that can be employed as excellent flexible bottom electrodes for highly efficient top-illuminated FOSCs. When an optimized 1-nm-thick Ag layer was deposited on the graphite film, the electrode exhibited high reflectance of visible light between 400 and 800 nm and ultralow sheet resistance. At the same time, the material costs are much lower than those of conventional opaque metal films. Additionally, the presented electrode system is highly flexible, with an almost constant conductivity down to a bending radius of 4 mm, showing great potential of replacing these metal electrodes for low-cost, reliable, and roll-to-roll processing. Single-junction, top-illuminated PTB7-Th: $PC_{71}BM$-based FOSCs employing Ag NP-modified graphite film as bottom electrode showed superior performance and achieved 5.31% efficiency. It was shown that the modified electrodes investigated in this study can replace the Ag film and fill the lack of high-performance flexible, opaque, conductive bottom electrodes, which are particularly important for large-area roll-to-roll-processed OSCs. Furthermore, based on the graphite bottom electrode, all-solution-processed FOSCs were fabricated using Ag NWs as the top electrode, and the impressive performance of the solar cell with a PCE of up to 3.76% was demonstrated. The stability and flexibility of the fully solution-processed, top-illuminated FOSCs were also greatly enhanced, and the good heat-insulation properties of graphite-based the FOSC were demonstrated. The novel design concept presented in this work is expected to open a new avenue for the penetration of cost-efficient FOSCs toward commercialization.

4 Experimental section

4.1 General information

Chlorobenzene, molybdenum oxide (MoO_x) (99.99%), and ZnO NPs/ethanol solution were obtained from Sigma Aldrich (St. Louis, MO, USA). Poly(3, 4-ethylen-edioxy-thiophene) doped with poly(styrenesulfonate) (PDEDOT:PSS) was obtained from Heraeus, Germany. Ag NW solution was purchased from BlueNano Company (Cornelius, NC, USA), with the average diameter of 90 nm and length of 30 μm. PTB7-Th and $PC_{71}BM$ were purchased from Luminescence Technology Corp. (Taiwan, China). All chemicals and regents were used as received from commercial sources without any further treatment.

4.2 Fabrication of bottom graphite electrode

Graphite thin-film electrode was fabricated following the processes described in our previous work [46]. The graphite substrate was cleaned by soaking it in concentrated sulfuric acid for 20 min. PDMS base and cross-linker were mixed in the weight ratio of 10:1, and the mixture was stirred for 1 h to remove the air bubbles in the solution. Subsequently, the PDMS layer was spin-coated on the PET substrates (2.6×3.1 cm²) and cured at 80°C for 5 h in air. The thin-film graphite electrode was patterned using a millimeter cutting machine, and the patterned thin-film graphite electrode was then transferred onto the PDMS film. In the patterning process, a photoresist spacing layer was spin-coated on the graphite surface to prevent contact between the graphite film and the compressor. The graphite electrode was covered by two clean glass substrates, and the sandwich structure was transferred onto the compressor. A flat-plate pressure of 0.6 MPa for 60 s was applied to embed the graphite into the soft PDMS layer. After pressing, the photoresist spacing layer was removed using acetone, and the prepared graphite films were dried at 90°C for 1 h. The Ag film was then deposited on graphite by evaporation in a high-vacuum thermal evaporation chamber. The layer thickness was precisely controlled in situ by using a quartz crystal monitor. Preparation of the PET-PDMS/graphite substrate is schematically illustrated in Figure 1. The surface images of ultrathin, Ag-modified thin-film graphite electrodes were recorded using a scanning electron microscope (HITACHI S-4800). The sheet resistance (R_s) was measured with a four-point probe, while the reflectance spectra were measured under standard measurement conditions on a 7-SCSpec solar cell measurement system (7-STAR Co., Japan).

4.3 Fabrication of top Ag NWs electrode

An isopropanol dispersion of Ag NWs (5 mg/mL) was spin-coated at 1000 rpm for 60 s on the PDMS film and then annealed at 80°C for 30 min. The PDMS mold was prepared based on the method described in the previous work. Then, PEDOT: PSS was spin-coated on top of the Ag NWs film on the PDMS mold. The electrode was contacted with copper foil. Finally, the entire architecture was transferred and pressed using a variable-pressure press from the top of the active layer.

4.4 Fabrication and characterization of FOSCs

The PTB7–Th: $PC_{71}BM$ blend solution was prepared by dissolving 10 mg of PTB7-Th and 15 mg of $PC_{71}BM$ in 1 mL of

chlorobenzene. This solution was mixed with 3% ODCB (volume ratio) and stirred at 60°C for 24 h in a nitrogen-purged glove box with O_2 and H_2O levels <0.01 ppm. For the fabrication of flexible OSCs, the PET substrates were cleaned in an ultrasonic bath sequentially with deionized water, ethanol, and isopropanol, each for 90 min. A ~40-nm-thick ZnO EEL layer was then spin-coated on the clean substrates using the ZnO NP/ethanol solution followed by annealing at 100°C for 20 min in air to remove the residual ethanol. The substrates were then transferred into a glove box, and a ~100-nm-thick PTB7-Th:$PC_{71}BM$ photoactive layer was deposited on the ZnO EEL using a spin-coating process in the glove box. Finally, the samples were transferred to a vacuum chamber with a base pressure of 1×10^{-6} mbar for deposition of MoO_x (5 nm) and Ag (12 nm) layers by thermal evaporation. The deposition rates for the MoO_x and Ag were typically 0.05 and 0.02 nm/s, respectively. The FOSC had an illumination area of 0.04 cm^2, defined by the overlap area between the graphite electrode and the upper contact. The results presented in this work are averaged from a set of 20 devices.

The current density versus voltage ($J–V$) characteristics of the top-illuminated FOSCs were measured using a programmable source meter (Keithley 2400) under illumination of 100 mW/cm^2 with AM 1.5G simulated solar spectrum from a solar simulator. The EQE spectra of the devices were measured under standard measurement conditions on a 7-SCSpec solar cell measurements system. Thermal images were recorded by an infrared camera (FLIR T630sc). The FOSCs were not encapsulated, and the measurements were conducted under ambient conditions. The mechanical flexibility of the FOSCs was measured using a custom-made bending test system.

4.5 Optical simulation of nanostructures

FDTD simulations were performed using a commercially available package from Optiwave to simulate the optical absorption of the samples. The OptiFDTD software is based on the FDTD algorithm proposed by Yee in 1966 and was applied in our previous work [47, 48], which introduced a modeling technique with second-order central differences to solve the Maxwell equations by applying a finite difference approach. The FDTD algorithm can directly calculate the value of E (the electric field intensity) and H (the magnetic field intensity) at different points of the computational domain. The excitation field is a Gaussian-modulated continuous wave with the center wavelength of 550 nm.

Conflict of interest: The authors declare no competing financial interests.

References

[1] Tang CW. Two layer organic photovoltaic cell. Appl Phys Lett 1986;48:183–5.

[2] Kaltenbrunner M, White M, Głowacki E, et al. Ultrathin and lightweight organic solar cells with high flexibility. Nat Commun 2012;3:770.

[3] Hou J, Inganäs O, Friend R. Gao, F. Organic solar cells based on non-fullerene acceptors. Nat Mater 2018;17:119–28.

[4] Cheng P, Li G, Zhan X, Yang Y. Next-generation organic photovoltaics based on non-fullerene acceptors. Nat Photonics 2018;12:131–42.

[5] Chen JD, Cui C, Li YQ, et al. Single-junction polymer solar cells exceeding 10% power conversion efficiency. Adv Mater 2015;27:1035–42.

[6] Lu H, Zhang D, Ren X, Liu J, Choy WC. Selective growth and integration of silver nanoparticles on silver nanowires at room conditions for transparent nano-network electrode. ACS Nano 2014;8:10980–7.

[7] McCoul D, Hu W, Gao M, Mehta V, Pei Q. Recent advances in stretchable and transparent electronic materials. Adv Electron Mater 2016;2:1500407.

[8] Huang H, Li X, Zhong L, et al. High performance as-cast semitransparent polymer solar cells. J Mater Chem A 2018;6:4670–7.

[9] Wang Y, Tong SW, Xu XF, et al. Interface engineering of layer-by-layer stacked graphene anodes for high-performance organic solar cells. Adv Mater 2011;23:1514–8.

[10] Chen D, Liang J, Liu C, et al. Thermally stable silver nanowire-polyimide transparent electrode based on atomic layer deposition of zinc oxide on silver nanowires. Adv Funct Mater 2015;25:7512–20.

[11] Cataldo S, Salice P, Menna E, Pignataro B. Carbon nanotubes and organic solar cells. Energy Environ Sci 2012;5:5919–40.

[12] Song Y, Chang S, Gradecak S, Kong J. Visibly transparent organic solar cells on flexible substrates with all graphene electrodes. Adv Energy Mater 2016;6:1600847.

[13] Wang J, Fei F, Luo Q, et al. Modification of the highly conductive PEDOT: PSS layer for use in silver nanogrid electrodes for flexible inverted polymer solar cells. ACS Appl Mater Interfaces 2017;9:7834–42.

[14] Wei B, Pan S, Wang T, et al. Solution-processed Ag-nanowire/ZnO-nanoparticle composite transparent electrode for flexible organic solar cells. Nanotechnology 2016;27:505208.

[15] Liu Z, Li J, Sun ZH, et al. The application of highly doped single-layer graphene as the top electrodes of semitransparent organic solar cells. ACS Nano 2011;6:810–8.

[16] Wang F, Chen Z, Xiao L, et al. Papery solar cells based on dielectric/metal hybrid transparent cathode. Sol Energy Mater Sol Cells 2010;94:1270–4.

[17] Hanmandlu C, Liu C, Chen CY, et al. Top illuminated hysteresis-free perovskite solar cells incorporating microcavity structures on metal electrodes: a combined experimental and theoretical approach. ACS Appl Mater Interfaces 2018;10:17973–84.

[18] Tyler M, Hutter O, Walker D, et al. A silver-free, reflective substrate electrode for electron extraction in top-illuminated organic photovoltaics. Chem Phys Chem 2015;16:1203–9.

[19] He Z, Zhong C, Su S, et al. Enhanced power-conversion efficiency in polymer solar cells using an inverted device structure. Nat Photonics 2012;6:591–5.

[20] Zhang M, Chiu TL, Lin CF, et al. Roughness characterization of silver oxide anodes for use in efficient top-illuminated organic solar cells. Sol Energy Mater Sol Cells 2011;95:2606–9.

[21] Xu WF, Pan MY, Fu PH, et al. Efficiency enhancement of top-illuminated ITO-free organic solar cells using plasmonic-assisted nanostructured reflective electrodes. J Mater Chem C 2015;3:9131–6.

[22] Ham J, Dong WJ, Park J, et al. A challenge beyond bottom cells: top-illuminated flexible organic solar cells with nanostructured dielectric/metal/polymer (DMP) films. Adv Mater 2015;27:4027–33.

[23] Schubert S, Müller L, Leo K. Unusually high optical transmission in Ca: Ag blend films: high-performance top electrodes for efficient organic solar cells. Adv Funct Mater 2014;24:6668–76.

[24] Tsai Y, Hong LA, Huang J, et al. Top-emission organic light emitting diode fabrication using high dissipation graphite substrate. Int J Photoenergy 2014;319390:1–6.

[25] Song R, Wang Q, Mao B, et al. Flexible graphite films with high conductivity for radio-frequency antennas. Carbon 2018;130:164–9.

[26] Tran VT, Saint J, Dollfus P, Volz S. High thermoelectric performance of graphite nanofibers. Nanoscale 2018;10:3784–91.

[27] Li YQ, Tan LW, Hao XT, et al. Flexible top-emitting electroluminescent devices on polyethylene terephthalate substrates. Appl Phys Lett 2005;86:153508-1-53508-3.

[28] Dong WJ, Ham J, Kim K, et al. Simple bar-coating process for fabrication of flexible top-illuminated polymer solar cells on metallic substrate. Adv Mater Technol 2016;1:1600128.

[29] Young CH, Chen YL, Chen PC. Heat insulation solar glass and application on energy efficiency buildings. Energy Build 2014;78:66–78.

[30] Cuce E, Young CH, Riffat SB. Performance investigation of heat insulation solar glass for low-carbon buildings. Energy Convers Manag 2014;88:834–41.

[31] Ando E, Suzuki S, Aomine N, et al. Sputtered silver-based low-emissivity coatings with high moisture durability. Vacuum 2000;59:792–9.

[32] Tong J, Yang X, Xu Y, et al. Efficient top-illuminated organic-quantum dots hybrid tandem solar cells with complementary absorption. ACS Photonics 2017;4:1172–7.

[33] Makha M, Testa P, Anantharaman S, et al. Ternary semitransparent organic solar cells with a laminated top electrode. Sci Technol Adv Mater 2017;18:68–75.

[34] Lian L, Dong D, Yang S, et al. Highly conductive and uniform alginate/silver nanowire composite transparent electrode by room temperature solution processing for organic light emitting diode. ACS Appl Mater Interfaces 2017;9:11811–8.

[35] Kirchartz T, Kaienburg P, Baran D. Figures of merit guiding research on organic solar cells. J Phys Chem C 2018;122:5829–43.

[36] Wang ZB, Helander MG, Qiu J, et al. Unlocking the full potential of organic light-emitting diodes on flexible plastic. Nat Photonics 2011;5:753–7.

[37] Sennett RS, Scott GD. The structure of evaporated metal films and their optical properties. J Opt Soc Am 1950;40:203.

[38] Krantz J, Stubhan T, Richter M, et al. Spray-coated silver nanowires as top electrode layer in semitransparent P3HT: PCBM-based organic solar cell devices. Adv Funct Mater 2013;23:1711–7.

[39] Barr MC, Howden RM, Lunt R, et al. Top-illuminated organic photovoltaics on a variety of opaque substrates with vapor-printed poly (3, 4-ethylenedioxythiophene) top electrodes and MoO_3 buffer layer. Adv Energy Mater 2012;2:1404–9.

[40] Lin HW, Chiu SW, Lin LY, et al. Device engineering for highly efficient top-illuminated organic solar cells with microcavity structures. Adv. Mater 2012;24:2269–72.

[41] Karg M, Konig T, Retsch M, et al. Colloidal self-assembly concepts for light management in photovoltaics. Mater Today 2015;18:185–205.

[42] An C, Yoo H, Cho C, et al. Surface plasmon assisted high performance top illuminated polymer solar cells with nanostructured Ag rear electrodes. J Mater Chem A 2014;2:2915–21.

[43] Liu Z, Li J, Yan F. Package-free flexible organic solar cells with graphene top electrodes. Adv Mater 2013;25:4296–301.

[44] Seo JH, Hwang I, Um HD, et al. Cold isostatic-pressured silver nanowire electrodes for flexible organic solar cells via room-temperature processes. Adv Mater 2017;29:1701479.

[45] Song W, Fan X, Xu B, et al. All-solution-processed metal-oxide-free flexible organic solar cells with over 10% efficiency. Adv Mater 2018;27:1800075.

[46] Wang S, Yang J, Xu X, et al. Highly efficient and foldable top-emission organic light-emitting diodes based on Ag-nanoparticles modified graphite electrode. Org Electron 2019;64:146–53.

[47] Yee K, Numerical solution of initial boundary value problems involving Maxwell's equations in isotropic media. IEEE Trans Antennas Propag 1966;14:302–7.

[48] Ibrahim E, Cristini R, Chen MY, et al. Local Schottky contacts of embedded Ag nanoparticles in Al_2O_3/SiNx: H stacks on Si: a design to enhance field effect passivation of Si junctions. Nanotechnology 2018;29:285403.